



# Time-resolved retardance and optic-axis angle measurement system for characterization of flexoelectro-optic liquid crystal and other birefringent devices

JULIAN A. J. FELLS,<sup>1,2</sup> STEVE J. ELSTON,<sup>1,3</sup> MARTIN J. BOOTH,<sup>1,4</sup> AND STEPHEN M. MORRIS<sup>1,5</sup>

<sup>1</sup>Department of Engineering Science, University of Oxford, Parks Road, Oxford, OX1 3PJ, UK

<sup>2</sup>julian.fells@eng.ox.ac.uk

<sup>3</sup>steve.elston@eng.ox.ac.uk

<sup>4</sup>martin.booth@eng.ox.ac.uk

<sup>5</sup>stephen.morris@eng.ox.ac.uk

**Abstract:** A new polarimeter is presented which gives time-resolved measurements of both the optic-axis angle and the linear phase retardation for modulated birefringent optical devices. It is suitable for characterizing dynamic waveplate devices based on liquid crystal and other materials. It is fully automated and requires no angular alignment of the device under test. The system has an absolute angle error of  $< \pm 0.3^\circ$  and a retardance error of  $< \pm 0.44^\circ$ , with considerably better relative accuracy. The method has been tested with a chiral nematic liquid crystal device exhibiting flexoelectro-optic switching at 3 kHz in the uniform lying helix mode. These results represent the first time-resolved tilt-angle and phase retardation measurements for a liquid crystal device operating at fast switching frequencies.

Published by The Optical Society under the terms of the [Creative Commons Attribution 4.0 License](https://creativecommons.org/licenses/by/4.0/). Further distribution of this work must maintain attribution to the author(s) and the published article's title, journal citation, and DOI.

**OCIS codes:** (120.5410) Polarimetry; (260.1440) Birefringence; (230.3720) Liquid-crystal devices; (120.4640) Optical instruments; (070.6120) Spatial light modulators.

## References and links

1. P. Rudquist, L. Komitov, and S. T. Lagerwall, "Volume-stabilized ULH structure for the flexoelectro-optic effect and the phase-shift effect in cholesterics," *Liq. Cryst.* **24**(3), 329–334 (1998).
2. T. J. Gould, D. Burke, J. Bewersdorf, and M. J. Booth, "Adaptive optics enables 3D STED microscopy in aberrating specimens," *Opt. Express* **20**(19), 20998–21009 (2012).
3. A. Jesacher and M. J. Booth, "Parallel direct laser writing in three dimensions with spatially dependent aberration correction," *Opt. Express* **18**(20), 21090–21099 (2010).
4. J. Chen, S. M. Morris, T. D. Wilkinson, J. P. Freeman, and H. J. Coles, "High speed liquid crystal over silicon display based on the flexoelectro-optic effect," *Opt. Express* **17**(9), 7130–7137 (2009).
5. J. S. Patel and R. B. Meyer, "Flexoelectric electro-optics of a cholesteric liquid crystal," *Phys. Rev. Lett.* **58**(15), 1538–1540 (1987).
6. R. M. A. Azzam, "Photopolarimetric measurement of the Mueller matrix by Fourier analysis of a single detected signal," *Opt. Lett.* **2**(6), 148–150 (1978).
7. S. R. M. Robertson, "Measuring birefringence properties using a wave plate and an analyzer," *Appl. Opt.* **22**(14), 2213–2216 (1983).
8. P. A. Williams, A. H. Rose, and C. M. Wang, "Rotating-polarizer polarimeter for accurate retardance measurement," *Appl. Opt.* **36**(25), 6466–6472 (1997).
9. K.-C. Lim and J. T. Ho, "Apparatus for high-resolution birefringence measurement in liquid crystals," *Mol. Cryst. Liq. Cryst. (Phila. Pa.)* **47**(3–4), 173–177 (1978).
10. I. G. Wood and A. M. Glazer, "Ferroelastic phase transition in BiVO<sub>4</sub>. I. Birefringence measurements using the rotating-analyser method," *J. Appl. Cryst.* **13**(3), 217–223 (1980).
11. J. Etxebarria, A. Remón, M. J. Tello, T. A. Ezcurra, M. A. Pérez-Jubindo, and T. Sierra, "A new method for high accuracy tilt angle measurements in ferroelectric liquid crystals," *Mol. Cryst. Liq. Cryst. (Phila. Pa.)* **150**(1), 257–263 (1987).
12. C. Noot, S. P. Perkins, and H. J. Coles, "Tilt angle measurement of low molar mass organosiloxane liquid crystals," *Ferroelectrics* **244**(1), 331–338 (2000).

13. G. Baur, V. Wittwer, and D. W. Berreman, "Determination of the tilt angles at surfaces of substrates in liquid crystal cells," *Phys. Lett.* **56A**(2), 142–144 (1976).
14. S.-T. Wu, U. Efron, and L. D. Hess, "Birefringence measurements of liquid crystals," *Appl. Opt.* **23**(21), 3911–3915 (1984).
15. P. Rudquist, M. Buivydas, L. Komitov, and S. T. Lagerwall, "Linear electro-optic effect based on flexoelectricity in a cholesteric with sign change of dielectric anisotropy," *J. Appl. Phys.* **76**(12), 7778–7783 (1994).
16. R. C. Jones, "A new calculus for the treatment of optical systems I. Description and discussion of the calculus," *J. Opt. Soc. Am.* **31**(7), 488–493 (1941).
17. J. J. Gil and E. Bernabeu, "Obtainment of the polarizing and retardation parameters of a non-depolarizing optical system from the polar decomposition of its Mueller matrix," *Optik (Stuttg.)* **76**(2), 67–71 (1987).
18. Specifications, "WPQ05M-546 - Ø1/2" Mounted Zero-Order, Quarter-Wave Plate, 546 nm," (Thorlabs Inc.) [https://www.thorlabs.com/newgrouppage9.cfm?objectgroup\\_id=7234](https://www.thorlabs.com/newgrouppage9.cfm?objectgroup_id=7234)
19. S. J. Elston, "Flexoelectricity in nematic domain walls," *Phys. Rev. E Stat. Nonlin. Soft Matter Phys.* **78**(1), 011701 (2008).
20. A. Varanytsia and L.-C. Chien, "Giant flexoelectro-optic effect with liquid crystal dimer CB7CB," *Sci. Rep.* **7**, 41333 (2017).
21. J. Li, C.-H. Wen, S. Gauza, R. Lu, and S.-T. Wu, "Refractive indices of liquid crystals for display applications," *J. Disp. Technol.* **1**(1), 51–61 (2005).
22. B. I. Outram and S. J. Elston, "Determination of flexoelectric coefficients in nematic liquid crystals using the crystal rotation method," *Liq. Cryst.* **39**(2), 149–156 (2012).
23. B. I. Outram and S. J. Elston, "Flexoelectric and dielectric in-plane switching behaviour of Grandjean liquid-crystal structures," *EPL* **99**(3), 37007 (2012).
24. H. Chen, R. Zhu, J. Zhu, and S.-T. Wu, "A simple method to measure the twist elastic constant of a nematic liquid crystal," *Liq. Cryst.* **42**(12), 1738–1742 (2015).

## 1. Introduction

Optical devices which allow their birefringent properties to be dynamically controlled have many technological applications. For example, they can be used to fabricate spatial light modulators (SLMs) [1], for use in optical microscopy [2], laser micromachining [3], and holography [4]. Liquid crystal (LC) devices are attractive for birefringent switching as they can be fabricated in planar arrays of pixels which are driven from an electrical backplane and used in a reflective configuration. Chiral nematic LC devices utilizing the flexoelectro-optic effect [5], are of particular interest for SLMs [1,4], as they are birefringent devices in which the angle of the optic-axis may be modulated with comparatively fast switching frequencies >1 kHz. For these devices a measurement of the optic-axis angle is needed.

Many polarimeters have been devised to measure the absolute retardance of optical devices with very high accuracy, for example, the Mueller matrix polarimeter [6], the rotating quarter-wave plate polarimeter [7], and the rotating polarizer polarimeter [8]. However, LC devices need more dedicated measurement systems to simultaneously measure both retardance and optic-axis angle under dynamic conditions. A feature of many LC devices is that they need to be driven with a bipolar electric field to prevent ionic screening effects. As they cannot be held in a static state, this precludes the use of polarimeters which rely on the polarization state remaining constant for the duration of the measurement.

One polarimeter which has been used for LC devices is the rotating analyzer [9–12], which has been used for a range of devices such as nematic LC [9], ferroelastic crystal [10], and ferroelectric LC [11,12]. In this method, circular polarized light is injected into the device under test (DUT) and the emergent light passes through a continuously rotating analyzer. The tilt-angle of the optic-axis of a chiral nematic LC, for example, may then be obtained by measuring the phase shift of the sinusoidal intensity signal, which is at twice the rotation frequency. However, a significant drawback with this approach is that there is a limit to which the analyzer may be safely rotated, thereby limiting the rotation frequency to around 100 Hz. This in turn limits the maximum frequency at which the device can be driven to around 10 Hz, as the modulation frequency applied to the LC must be significantly below the frequency of the sinusoidal signal. For example, a 1 Hz switching frequency was used in [12]. This presents a problem for the characterization of LC devices as ionic screening effects typically dictate that they need to be switched with drive frequencies of at least 100 Hz–1 kHz

to prevent the applied voltage dropping during the duration of each pulse. Employing the rotating analyzer method to measure the tilt-angle of the optic-axis during flexoelectro-optic switching in a chiral nematic LC is therefore likely to introduce considerable measurement error due to ionic screening effects.

As a result, LC devices are generally characterized by the intensity response when the device is placed between crossed polarizers [13–15]. For the case of the flexoelectro-optic effect, for example, the switching angle of the optic-axis is typically measured using a polarizing optical microscope equipped with a fast photodetector mounted on the phototube. A square-wave electric field is applied to the device and the response is then recorded on a digitizing oscilloscope. The magnitude of the tilt-angle (the deflection of the optic-axis for one polarity of the applied electric field) can then be determined by either rotating the sample [13,14], or by monitoring the modulation depth when the sample is at  $22.5^\circ$  to the transmission axis of one of the polarizers [15]. However, even when well-centered, rotating the sample inevitably results in the portion illuminated changing to some degree; the sample properties and thickness may not be uniform over this area.

The cross-polarizer measurement technique typically involves manual operation to align the sample on the rotation stage and take the measurements, which can be time-consuming, preventing high measurement throughput. The accuracy of this measurement is also limited because it is an intensity based system, which may be impacted by imperfect polarizers and optical source power variation. In addition, test samples may consist of multiple ‘domains’, whereby different domains have a different angle of the optic-axis, resulting in measurement error. The measurement method is also unable to adequately deconvolve changes in tilt-angle, birefringence and loss into separate components. In some samples, it is possible that all three of these parameters may change simultaneously, each with different time constants. The response may be further complicated by ionic screening effects which result in a reduction of the applied electric field over the pulse duration. In order to understand fully the device dynamics, it is therefore desirable to have a time-resolved measurement process so that all the parameters can be isolated from one another. In this paper, we present a new method for measuring the time-resolved angle of the optic-axis and the linear retardance under dynamic switching conditions, which overcomes the aforementioned limitations.

This paper is organized as follows: Section 2 explains the principle behind the new measurement technique followed by Section 3, which shows a novel error cancellation technique for compensating systematic error. Section 4 details the experimental set-up and explains the measurement procedure. Section 5 determines the accuracy of the system using a test waveplate. Section 6 shows results for a dynamically switched LC device, followed by Section 7 which validates the dynamic measurements against theory and other measurements. Section 8 examines the applicability of the technique to non-ideal devices. Finally, conclusions are presented in Section 9.

## 2. Principle of operation

The measurement system is illustrated diagrammatically in Fig. 1. A circularly polarized beam is generated by the laser (L), polarizer, (P1) and a quarter-wave plate (QWP). This light is then injected into the device under test (DUT), which is electrically driven with an arbitrary function generator (AFG). The DUT is considered to be optically equivalent to a waveplate with linear retardance,  $\delta(t)$ , and angle of the optic-axis,  $\varphi(t)$ . These properties vary with time under the stimulus from the AFG. The emergent light passes through an analyzer (P2) and is detected on a photodetector (PD). P2 is on a motorized rotation mount so that its angle,  $\theta$ , may be precisely adjusted to different static angles, to obtain the intensity component at each separate analyzer angle. This is different to the rotating analyzer systems described elsewhere [9–12], which use a continuously rotating analyzer.

A time-varying voltage with a repeating pattern is applied to the DUT. The output of the PD is digitally time-sampled using a data acquisition system, which is triggered on the input

voltage pattern. A series of time-sampled measurements are then taken at equally spaced analyzer angles. The intensity on the photodetector as a function of analyzer angle,  $\theta$ , and time,  $t$ , may be determined from [10], as

$$S(\theta, t) = \frac{1}{2} S_0 [1 + \sin(\delta(t)) \sin(2\theta - 2\varphi(t))] \quad (1)$$

where  $S_0$  is the input light intensity.

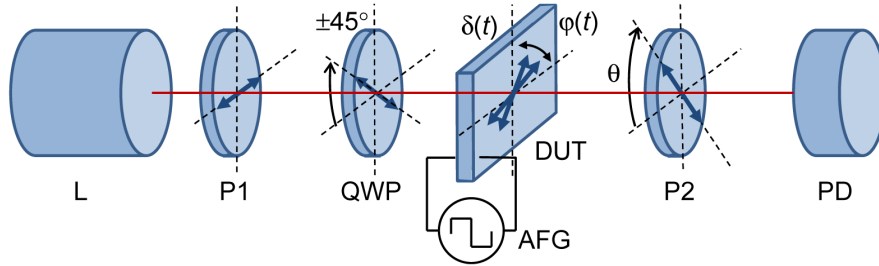


Fig. 1. Diagrammatic representation of the measurement system; L: Laser, P1: input polarizer, QWP: quarter-wave plate (on a motorized rotation mount), DUT: device under test, AFG: arbitrary function generator, P2 output polarizer (on a motorized rotation mount), PD: photodetector.

Measurements are taken at  $M$  discrete angles,  $\theta_m = 2\pi m/M$ , where  $m = \{0, 1, \dots, M-1\}$ . Each measurement has  $N$  time samples at times  $nT$ , where  $T$  is the sampling period and  $n = \{0, 1, \dots, N-1\}$ . Each time-sample is considered separately, to compute the angle of the optic-axis and retardance from the measurements at each angle. As the measurements at each analyzer angle are time-synchronized with one another,  $S(\theta)$  can be obtained at each time-sample point,  $n$ . From Eq. (1), the received signal is sinusoidal with phase  $2\varphi(nT)$ . As there will be exactly 2 periods of the recovered sinusoidal signal as  $\theta$  is rotated between 0 and  $2\pi$ , the phase can then be measured relative to a reference signal of  $\sin(2\theta)$  in order to recover  $\varphi(nT)$ . The angle of the optic-axis at an individual time-sample point is then determined from the phase shift over  $\theta$  of this signal. Similarly, the linear retardance,  $\delta(nT)$ , is obtained from the amplitude of the signal relative to the mean signal. A very accurate method of deducing these parameters is by phase-sensitive detection. However, in this case, the phase is relative to the analyzer angle,  $\theta$ , rather than over time. This means that simple averaging can be used for image rejection and a low noise bandwidth.

An in-phase signal is generated by multiplying  $S(\theta, t)$  by  $\sin 2\theta$  to obtain the sum and difference terms,  $-\frac{1}{4} S_0 \sin(\delta(t)) \cos(4\theta - 2\varphi(nT))$  and  $\frac{1}{4} S_0 \sin(\delta(t)) \cos(2\varphi(nT))$ , respectively, as well as  $\frac{1}{2} S_0 \sin 2\theta$ . Averaging over  $\theta$  leaves just the desired difference term. Similarly, a quadrature signal is formed by multiplying  $S(\theta)$  by  $-\cos 2\theta$  and averaging over  $\theta$  to give the difference term  $\frac{1}{4} S_0 \sin(\delta(t)) \sin(2\varphi(nT))$ . The in-phase,  $I(nT)$ , and quadrature,  $Q(nT)$ , values at time-sample  $n$  may then be written, respectively, as

$$I(nT) = \frac{1}{M} \sum_{m=0}^{M-1} \sin(2\theta_m) S(\theta_m, nT) \quad (2)$$

$$Q(nT) = \frac{-1}{M} \sum_{m=0}^{M-1} \cos(2\theta_m) S(\theta_m, nT) \quad (3)$$

The measured angle of the optic-axis,  $\varphi_M(nT)$ , and retardance,  $\delta_M(nT)$ , at time-sample  $n$  may then be written, respectively, as

$$\varphi_M(nT) = \frac{1}{2} \tan^{-1} \left( \frac{Q(nT)}{I(nT)} \right) \quad (4)$$

$$\delta_M(nT) = \sin^{-1} \left( \frac{2 \left[ Q(nT)^2 + I(nT)^2 \right]^{1/2}}{\overline{S(nT)}} \right) \quad (5)$$

where  $\tan^{-1}()$  is a four-quadrant arctangent function and  $\overline{S(nT)}$  is the mean signal over  $\theta_m$  at sample  $n$ , given by

$$\overline{S(nT)} = \frac{1}{M} \sum_{m=0}^{M-1} S(\theta_m, nT) \quad (6)$$

Equations (4) and (5) can therefore be used to compute the optic-axis angle (relative to the horizontal) and linear retardance, respectively, for each time sample, thereby providing time resolved measurements. Additionally, Eq. (6) allows the variation in transmission loss with time to be determined.

### 3. Error analysis and cancellation scheme

It has been found that in a practical implementation, there is a systematic error associated with the non-ideality of the QWP used to generate the input circularly polarized light. Commercially available QWPs have retardance tolerances ranging through  $\pm \lambda/300$  (Thorlabs, Newport),  $\pm \lambda/350$  (Edmund) to  $\pm \lambda/500$  (Linos) and this can have a significant impact. In order to analyze this error, a Jones Matrix approach [16], was used. The DUT is represented by a linear retarder,  $\mathbf{W}_D$ , with retardance  $\delta(t)$  and optic axis  $\varphi(t)$  to the horizontal. The QWP is represented by a linear retarder,  $\mathbf{W}_Q$ , with a retardance error of  $\epsilon$  from  $\pi/2$ . It is at an angle of  $\pi/4 + \zeta_L$  to the horizontal for left-circular polarization (LCP) or  $-\pi/4 + \zeta_R$  for right-circular polarization (RCP), where  $\zeta_L$  and  $\zeta_R$  are angular errors in the setting of the QWP. The received intensity after the polarizer may be written for LCP and RCP, respectively, as

$$S_L(\theta, t) = S_0 \left| \mathbf{P}(\theta) \mathbf{W}_D(\delta(t), \varphi(t)) \mathbf{W}_Q(\pi/2 + \epsilon, \pi/4 + \zeta_L) \mathbf{E}_H \right|^2 \quad (7)$$

$$S_R(\theta, t) = S_0 \left| \mathbf{P}(\theta) \mathbf{W}_D(\delta(t), \varphi(t)) \mathbf{W}_Q(\pi/2 + \epsilon, -\pi/4 + \zeta_R) \mathbf{E}_H \right|^2 \quad (8)$$

where  $\mathbf{E}_H = [1 \ 0]^T$  is the well-known Jones vector for a horizontal polarization input optical field and  $\mathbf{P}(\theta) = [\cos\theta \ \sin\theta]$  takes the optical field amplitude component aligned to a polarizer at angle  $\theta$  with the horizontal. The Jones matrices for the linear retarders  $\mathbf{W}_D(\gamma, \beta)$  and  $\mathbf{W}_Q(\gamma, \beta)$ , with retardance  $\gamma$  and optic-axis angle  $\beta$  with the horizontal, are represented by [17],

$$\mathbf{W}_{D,Q}(\gamma, \beta) = \begin{bmatrix} \cos(\gamma/2) + j \cos 2\beta \sin(\gamma/2) & j \sin 2\beta \sin(\gamma/2) \\ j \sin 2\beta \sin(\gamma/2) & \cos(\gamma/2) - j \cos 2\beta \sin(\gamma/2) \end{bmatrix} \quad (9)$$

Solving Eqs. (7) and (8) assuming  $\epsilon$ ,  $\zeta_L$  and  $\zeta_R$  to be small yields

$$S_L(\theta, t) = \frac{1}{2} S_0 \left[ 1 + \sin(\delta(t)) \sin(2\theta - 2\varphi(t)) + \epsilon R_1(\theta, t) + \zeta_L R_2(\theta, t) \right] \quad (10)$$

$$S_R(\theta, t) = \frac{1}{2} S_0 \left[ 1 - \sin(\delta(t)) \sin(2\theta - 2\varphi(t)) + \epsilon R_1(\theta, t) + \zeta_R R_2(\theta, t) \right] \quad (11)$$

where  $R_1(\theta, t)$  and  $R_2(\theta, t)$  are given by



$$R_1(\theta, t) = \sin(2\theta - 2\varphi(t)) \sin 2\varphi(t) \cos \delta(t) - \cos(2\theta - 2\varphi(t)) \cos 2\varphi(t) \quad (12)$$

$$R_2(\theta, t) = 2 \cos(2\theta - 2\varphi(t)) \left[ \sin(2\varphi(t)) \cos(\delta(t)) + \sin(\delta(t)) \right] \\ + 2 \sin(2\theta - 2\varphi(t)) + 2 \cos(2\varphi(t)) \sin(\delta(t)) \quad (13)$$

Equation (10) is similar to Eq. (1), except that, both the QWP retardance error,  $\epsilon$ , and QWP angle error  $\zeta_L$  give rise to additional terms in Eqs. (12) and (13). Terms in  $\sin(2\theta - 2\varphi)$  and  $\cos(2\theta - 2\varphi)$  lead to an additional phase shift,  $-2\varphi_e$ , in  $S(\theta, t)$  over  $\theta$ , where  $\varphi_e$  is a resulting systematic angle measurement error. This error,  $\varphi_e$ , varies with the actual angle,  $\varphi$ , with period  $\pi$ . For a QWP at exactly  $45^\circ$ , the maximum value of  $\varphi_e$  can be approximated from Eqs. (10) and (12) as

$$\varphi_{45, \epsilon, \max} = \pm \left| \frac{\epsilon}{2 \sin \delta_n} \right| \quad (14)$$

where  $\delta_n$  is the nominal retardance of the DUT. The error increases as the retardance of the DUT approaches a half- or full-wave plate. Equation (14) shows that even the best QWP with  $\pm \lambda/500$  tolerance will add potential error ranging from  $\pm 0.36^\circ$  for a DUT of  $0.25\lambda$ , increasing to  $\pm 5.7^\circ$  for a DUT of  $0.49\lambda$ . Any angle error,  $\zeta_L$ , in the QWP will serve to increase this value. There is also a corresponding periodic error in the retardance measurement through the change in fringe amplitude of  $S(\theta, t)$  over  $\theta$ .

In order to mitigate the systematic error, a novel cancellation scheme has been devised. By taking measurements with both LCP and RCP, it is possible to cancel the error terms by assuming  $\zeta_L = \zeta_R$ . By combining Eqs. (10) and (11), Eqs. (2), (3) and (6) may then be rewritten in terms of  $S_L(\theta, t)$  and  $S_R(\theta, t)$  as

$$I(nT) = \frac{1}{2M} \sum_{m=0}^{M-1} \sin(2\theta_m) [S_L(\theta_m, nT) - S_R(\theta_m, nT)] \quad (15)$$

$$Q(nT) = \frac{-1}{2M} \sum_{m=0}^{M-1} \cos(2\theta_m) [S_L(\theta_m, nT) - S_R(\theta_m, nT)] \quad (16)$$

$$\overline{S(nT)} = \frac{1}{2M} \sum_{m=0}^{M-1} [S_L(\theta_m, nT) + S_R(\theta_m, nT)] \quad (17)$$

Equations (15)-(17) may therefore be used with Eqs. (4)-(5) to calculate the angle of the optic-axis and retardance as before, but with the cancellation of the systematic error. There will be a residual error determined by the relative accuracy of the QWP rotation mount,  $\zeta_L - \zeta_R$ . However, this will be much smaller than the absolute accuracy of the QWP angular setting.

Numerical simulations are shown in Fig. 2, to check the cancellation without small angle approximation under different conditions (i) to (iv), selected to be commensurate with the experimental conditions in Section 5. Figure 2(a) shows the measurement angle error (deviation between the measured angle and actual angle) as the DUT angle of optic-axis is rotated through  $360^\circ$ . Figure 2(b) shows the corresponding error in measured optical retardance as the optic-axis is rotated. For conditions (i)-(iii), The DUT is a waveplate of  $0.4284\lambda$  retardance. In (i), the QWP has a retardance error of  $\lambda/400$  and there is no error in QWP angular alignment to set LCP and RCP. There is up to  $\pm 1.04^\circ$  of measurement angle error irrespective of whether LCP or RCP is used. However, when the LCP and RCP measurements are combined, there is perfect cancellation to the limit of numerical accuracy. The retardance measurement shows similar behavior, also exhibiting perfect cancellation. In

(ii) there is additionally an error in the angle of the QWP used to generate LCP light of  $0.4^\circ$ . However, to switch polarization, the QWP is rotated through exactly  $90^\circ$ . Here the measurement angle error has increased to  $\pm 1.38^\circ$  for both LCP and RCP light. However, again the combined LCP/RCP has perfect cancellation, for both angle and retardance measurements. In (iii) there is additionally an error in the QWP angle moved when switching between LCP light and RCP light. This relative QWP angle error is much smaller at  $0.07^\circ$  as the relative accuracy of modern rotation mounts is considerably better than their absolute accuracy. The LCP measurement angle error remains the same, but the RCP error increases to  $\pm 1.50^\circ$ . There is now imperfect cancellation for both angle and retardance measurements, but this is very small (angle measurement error of  $\pm 0.08^\circ$ ). Condition (iv) shows the effect of measuring a DUT with a retardance of  $0.49\lambda$ , with a high tolerance ( $\lambda/500$ ) QWP having no angle error. Here there is a larger measurement angle error of  $\pm 5.77^\circ$ , close to  $\pm 5.73^\circ$  predicted by Eq. (14), but there is still perfect cancellation for both angle and retardance measurements. The simulations therefore show that the cancellation technique mitigates both QWP retardance error and QWP angle error. It is, however, necessary to minimize the relative angular error when adjusting the QWP angle to change between setting LCP light and RCP light.

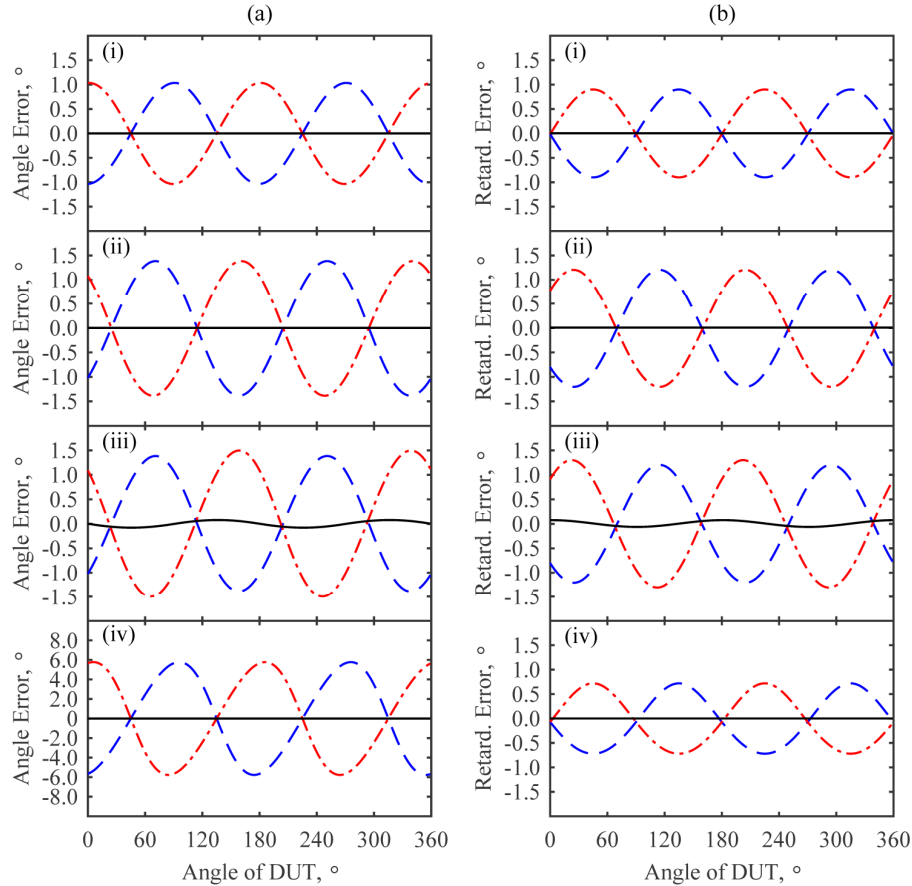


Fig. 2. Simulated measurement error for (a) angle of the optic-axis and (b) retardance; (— blue) LCP input, (--- red) RCP input, (— black) combined LCP/RCP inputs; (i) DUT  $0.4284\lambda$ , QWP error  $\lambda/400$ ; (ii) DUT  $0.4284\lambda$ , QWP error  $\lambda/400$ , QWP angle error  $0.4^\circ$ ; (iii) DUT  $0.4284\lambda$ , QWP error  $\lambda/400$ , QWP angle error  $0.4^\circ$  and  $0.07^\circ$  error switching from LCP to RCP; (iv) DUT  $0.49\lambda$ , QWP error  $\lambda/500$ .

#### 4. Experimental set-up and procedure

The experimental setup is as shown in Fig. 1. The light source used in this study was a continuous wave helium neon (He-Ne) laser at  $\lambda = 632.8$  nm (Uniphase 1135P) attenuated to 1 mW with a neutral density filter. The light passes through a Glan-Taylor polarizer (Thorlabs GT5-A) with  $>10^5$  extinction. This in turn passes through a QWP (Thorlabs WPQ05M-633) on a motorized rotation mount (Thorlabs K10CR1/M). The DUT was mounted on a hot-stage (Linkam LTS350 with TP93 controller) with an aperture of 2 mm. After the DUT there was a  $\sim 1$  mm aperture. The DUT was driven by an AFG (Wavetek 195).

The analyzer that was used in this study was a nanoparticle polarizer (Thorlabs LPVISC050-MP2) with  $>10^5$  extinction, on a motorized rotation mount (Thorlabs PRM1/MZ8 with KDC101). It was found that prism-based polarizers such as Glan-Taylor devices gave erroneous measurements, which is likely due to the unwanted beam-steering effect that they give. However, the nanoparticle polarizer was able to give equally high extinction without suffering from this drawback. The light from the analyzer was detected on a photodetector (Thorlabs PDA55) and the signal was digitally sampled with a 16-bit, 100 kS/s data acquisition card (National Instruments PCI-6033E) within a Personal Computer (PC). This was triggered from the 'sync' output from the AFG. The time resolution is limited only by the sampling rate and higher sampling rate cards may be used. In addition, a tap was used to monitor the input laser power, prior to the first polarizer. This consisted of a polarization beam splitter nominally aligned to the input polarization state for the through path, resulting in a small proportion of the light being tapped off in the reflected path.

To set up the system, the DUT was removed and replaced with a polarization analyzer (Schäfter + Kirchhoff SK010PA-VIS). This was used to set the polarization output as close as possible to LCP, by adjusting the angle of the QWP. There is a small offset because of the retardance error of the QWP. It was not desirable to move the QWP away from normal incidence to try and improve this (by altering the effective thickness) as we require the magnitude of the error to be the same for both LCP and RCP. The angle setting required for LCP is then recorded and stored as a parameter in the control software. The motorized mount was then rotated through  $90^\circ$  to check that the light was RCP.

All of the instrumentation was PC controlled using Matlab<sup>®</sup>. The temperature of the hot-stage was selected and the AFG was programmed to any arbitrary waveform that was desired. It was possible to perform separate measurements at a range of different voltage amplitudes and frequencies. However, this resulted in large amounts of time being required to complete the measurements. A more efficient approach was to program the AFG with a repeating pattern which consisted of a range of voltage amplitudes and frequencies, random pulse sequences and systematic pulse sequences. Using this pattern meant that from a single set of measurements over angle,  $\theta$ , a wide range of different drive conditions could be explored. The measurement time was typically around 12 minutes to cover 10 voltage amplitudes at a single temperature. However, if shorter measurement times are required, then this can be reduced by only taking measurements over half of the range of angles ( $0-\pi$ ) as this will still equate to a whole period of the signal. It is also possible to have larger angle increments.

The software first converts the input laser beam to LCP light and then takes 72 measurements at analyzer angles between  $0^\circ$  and  $355^\circ$  in  $5^\circ$  increments. It then takes the same 72 measurements for RCP light. These are then stored to disk in a 2-dimensional matrix, such that each row is a measurement at a different angle,  $\theta_m$ , and each column represents a different time-sample,  $n$ . Each column was then processed to compute  $I(nT)$ ,  $Q(nT)$ , and  $S(nT)$  using Eqs. (15)-(17) from the measurement data. Then the angle,  $\varphi_M(nT)$  and retardance,  $\delta_M(nT)$  are obtained from Eqs. (4)-(5), respectively. The angle,  $\varphi_M(nT)$  is phase unwrapped.



## 5. Calibration

To calibrate the system, a test waveplate of known retardance was used for the DUT. In order to show that the calibration is valid for arbitrary retardance, a half-waveplate at  $\lambda = 546$  nm was used (Thorlabs WPH05M-546). According to the manufacturer's specifications [18], this waveplate had a retardance of  $0.4298\lambda \pm \lambda/300$  at  $\lambda = 632.8$  nm. The waveplate was also mounted on a motorized rotation mount (Newport SR50PP with ESP300). As the test wave plate was not electrically switchable, the measurement data was averaged over time to give static measurements.

Figure 3 shows the experimentally captured raw intensity data as the test waveplate was rotated. The phase of the fringes shift with test waveplate angle for both LCP and RCP input light. There is also a small change in the fringe amplitude indicating a change in the measured phase retardance (including as a result of error due to the imperfect QWP as discussed above).

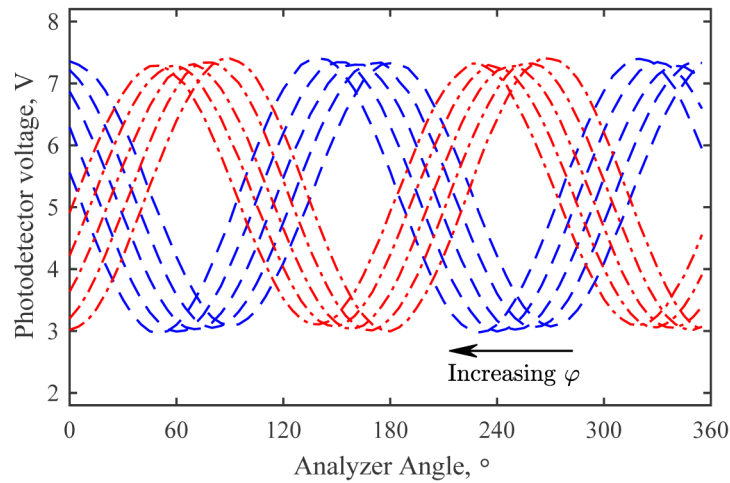


Fig. 3. Photo-detector voltage versus analyzer angle,  $\theta$ , for test wave plate angles of  $\varphi = 0-40^\circ$  in  $10^\circ$  increments; (— blue) LCP input, (— red) RCP input.

Figure 4 shows the experimentally determined properties for the test waveplate. Figure 4(a) shows the error in the measured angle from the actual angle of the test waveplate for both LCP and RCP light using Eqs. (2)-(4) and for the combination using Eqs. (4), (15) and (16). For both LCP and RCP light there is a periodic error dependent on the actual absolute angle of approximately  $\pm 1.5^\circ$ . However, the combination using both LCP and RCP has reduced this error to  $< \pm 0.3^\circ$ . The residual error is due to imperfect cancellation which may be partly due to error in the relative angle shift of the QWP to swap between LCP and RCP. However, it should be noted that this error will also include variation in the motorized mount for the test waveplate, which had a unidirectional repeatability of  $0.01^\circ$ . For many applications, it is the change in angle which is of interest; Fig. 4(a) shows that the relative accuracy improves as the angle excursion reduces.

Figure 4(b) shows the error in the measured retardance from the nominal retardance of  $154.217^\circ$ . Similarly there is a periodic error in both the LCP and RCP measurements. There is also a slow variation with a single period over  $0-360^\circ$ . Again, the combination of LCP and RCP has cancelled the periodic error, leaving a residual error of  $\pm 0.44^\circ$  (assuming the actual retardance is midway between the retardance variation). However, it is possible that some of this variation is due to non-flatness in the waveplate resulting in the retardance varying with angular position, rather than measurement error. Notwithstanding this, the measured retardance including this variation is well within the manufacturer's tolerance specification.

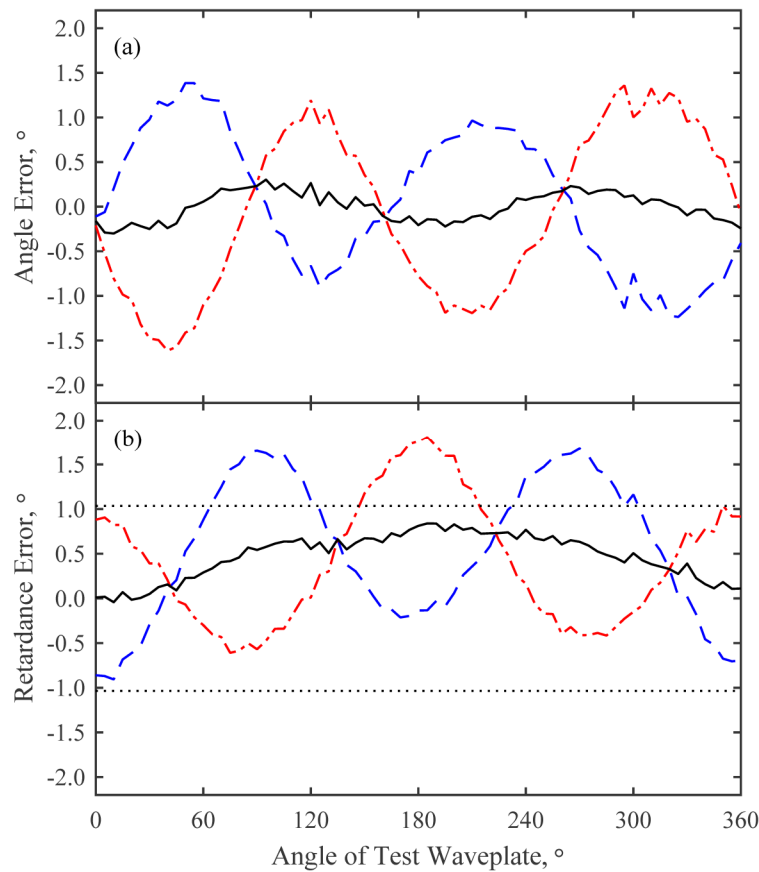


Fig. 4. Experimental calibration results using test wave plate on a motorized rotation mount; (a) error in measured angle from actual angle; (b) error in retardance (from nominal value of  $154.217^\circ$ ); (--- blue) LCP input, (-.-.- red) RCP input, (— black) combined LCP/RCP inputs, (..... black) limits of manufacturer's retardance tolerance specification.

The polarization analyzer has an absolute polarization angle accuracy of  $< \pm 0.2^\circ$  and the absolute error of the motorized QWP is  $< \pm 0.2^\circ$ . Taking worst-case figures, the absolute angular error in the QWP used to set LCP light is  $< 0.4^\circ$ . However, the relative accuracy of the motorized QWP is considerably better at  $0.07^\circ$ . The simulation results shown in Fig. 2(a)(iii) and Fig. 2(b)(iii) use these same error figures. Figure 2(a)(iii) shows very close correlation to the experimental results in Fig. 4(a). Figure 2(b)(iii) also shows correlation with Fig. 4(b) if the slow variation in retardance is neglected.

## 6. Liquid crystal device under dynamic switching

The measurement method is particularly attractive for characterizing chiral nematic flexoelectro-optic LC devices in the uniform lying helix (ULH) mode, the structure of which is illustrated in Fig. 5. Figure 5(a) shows diagrammatically a side-on view of a chiral nematic ULH device in a glass cell. The inside surfaces of the cell have indium tin oxide (ITO) electrodes and an alignment layer to facilitate the orientation of the LC structure. The LC material consists of rod-shaped (nematic) molecules which form a helical (chiral) structure. The molecules orient themselves perpendicular to the helix-axis with a molecular direction which rotates about the helix-axis along its length. In the ULH mode, the helix axis is 'lying down', oriented parallel to the cell surfaces and perpendicular to the light path.

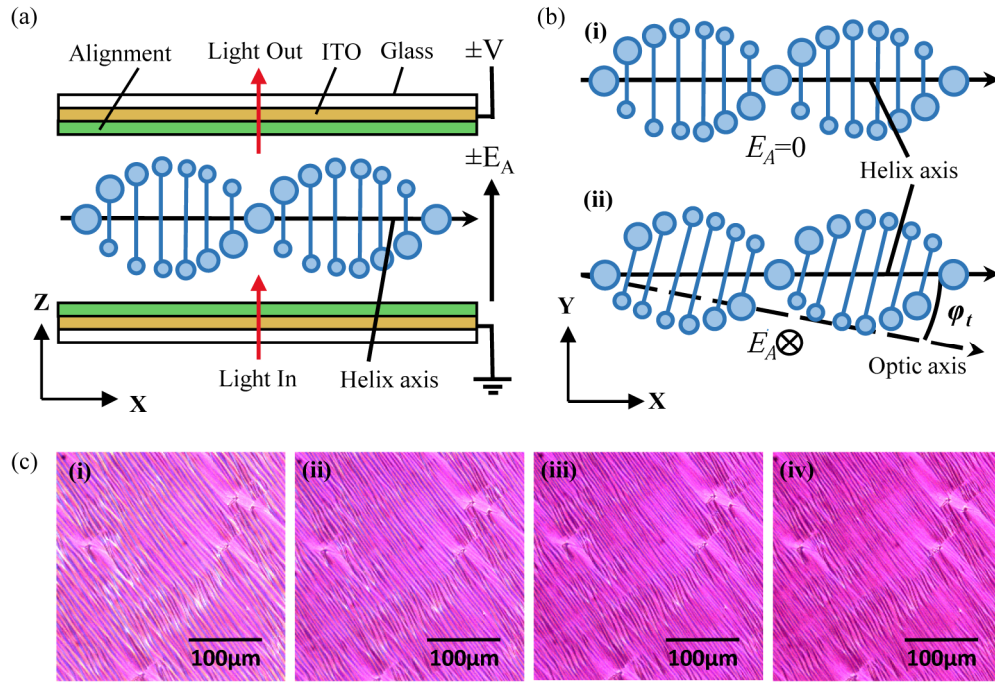


Fig. 5. The chiral nematic LC device used to validate the measurement system; (a) illustration of the ULH mode, (b) illustration of the flexoelectro-optic effect, (c) polarizing optical microscope images for sample with mean optic-axis at  $22.5^\circ$  to the axis of one of the polarizers, under an applied 1 kHz square-wave: (i)  $\pm 5$  V, (ii)  $\pm 10$  V, (iii)  $\pm 15$  V, (iv)  $\pm 20$  V. The device consists of 3.5 wt% chiral dopant (R5011) in the nematic host E7. The thickness of the device was  $4.82 \mu\text{m}$  and measurements were taken at  $25^\circ\text{C}$ . The discontinuities in the structure are due to the presence of spacer beads.

Figure 5(b) shows a view through the surface of the ULH device for (i) no applied electric field and (ii) with an applied electric field. The ULH mode is birefringent and light passing through the cell normal to the surfaces will experience a retardance with an optic-axis which is in the direction of the helix-axis. When an electric field is applied, the coupling between the applied field and field-induced flexoelectric polarization leads to a bend-splay distortion in the nematic director. This results in a rotation of the director plane around an axis parallel to the applied field. The molecules tilt, as shown in Fig. 5(b)(ii), causing a change in the optic-axis of the retardance. An approximate relationship (valid for the small tilt angles observed in this study) between the electric field applied to the sample,  $E_A$  and the tilt-angle,  $\phi_t$  is given by [5],

$$\tan(\phi_t) = \frac{e_1 - e_3}{K_{11} + K_{33}} \frac{p}{2\pi} E_A \quad (18)$$

where  $e_1$  and  $e_3$  are the splay and bend flexoelectric coefficients, respectively,  $K_{11}$  and  $K_{33}$  are the elastic constants for splay and bend respectively, and  $p$  is the chiral pitch of the helical structure. The angular change in optic-axis follows the polarity of the applied field and can be relatively fast (e.g.  $< 100 \mu\text{s}$ ). However, for large tilt-angles, a better approximation for the tilt-angle with applied field is provided in [19]. Tilt-angles  $> \pm 45^\circ$  have been observed for bimesogen mixtures [20]. A generally unwanted side-effect, is that there can be coupling of the electric field to the dielectric anisotropy of the chiral nematic LC, such that there is distortion in the helical structure and the helix starts to unwind. This would result in a reduction in the birefringence occurring simultaneously with the change in optic-axis,

complicating the dynamic response. Unlike the tilt-angle, this effect is insensitive to the polarity of field, and is only determined by the field magnitude. ULH devices can therefore be represented by the DUT in Fig. 1.

In order to demonstrate the measurement method, a chiral nematic LC with a well-known nematic host was prepared. The LC chosen for this study consisted of the nematic mixture, E7 (Synthon) dispersed with 3.5 wt% of a high twisting power chiral dopant (Merck R5011). Following thermal mixing, the mixture exhibited a chiral nematic phase from 55.6°C on cooling from the isotropic liquid phase. This mixture was capillary filled into a nominally 5  $\mu\text{m}$ -thick glass cell with antiparallel rubbed polyimide alignment layers and ITO electrodes. Prior to filling the cell, the cell thickness was determined to be 4.82  $\mu\text{m}$ , using a UV-VIS spectrometer to measure the Fabry-Perot fringes.

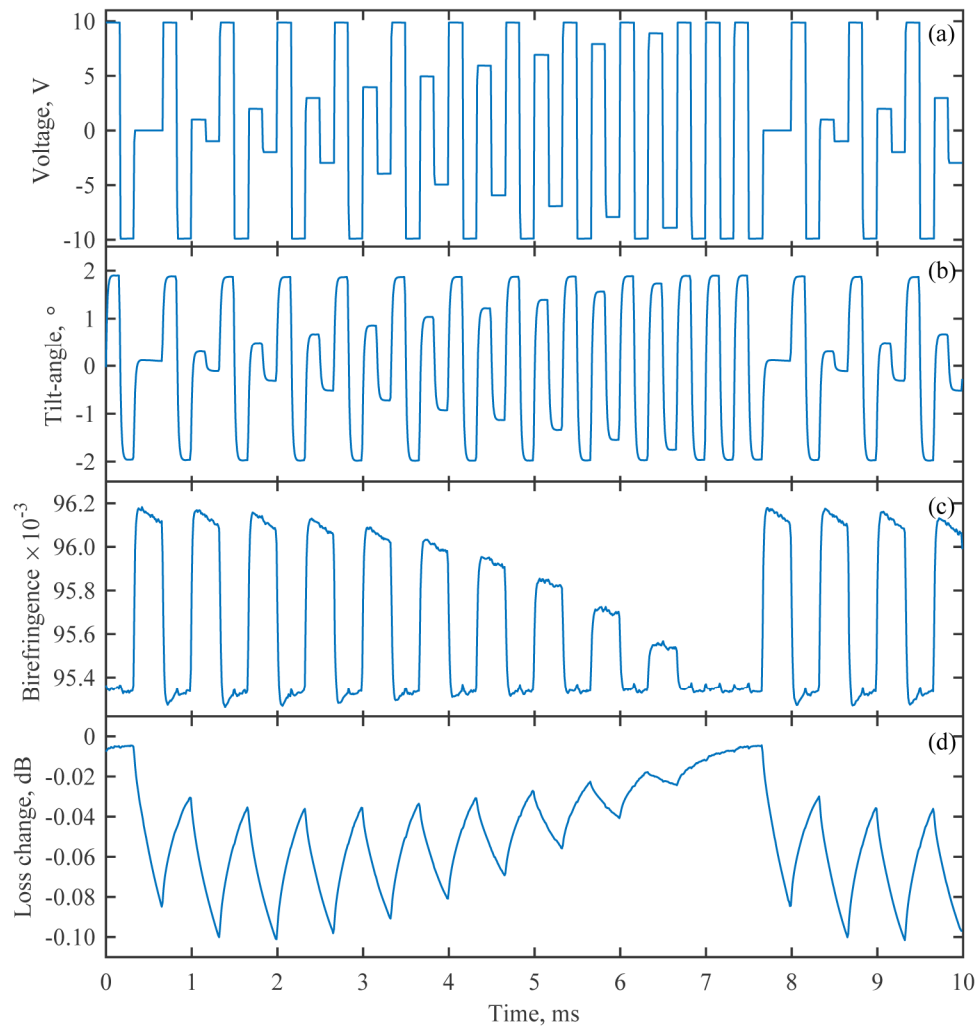


Fig. 6. Experimental time-resolved measurement data for a dynamically switched flexoelectro-optic LC device. (a) input voltage waveform; (b) tilt-angle, (c) linear birefringence; (d) loss change. The chiral nematic LC device consists of 3.5 wt% chiral dopant (R5011) in the nematic host E7. The thickness of the device was 4.82  $\mu\text{m}$  and measurements were taken at 25°C.

The cell was initially aligned in the Grandjean texture (helix-axis parallel to the surface normal of the glass substrates) and the white-light transmission spectrum recorded, showing a

long bandedge at around 340 nm. From this, the chiral pitch was estimated to be 173 nm (the extraordinary refractive index for E7 was extrapolated to 1.97 for this wavelength using a Cauchy model [21]). The cell was then aligned in the ULH mode by heating above the clearing temperature and allowing it to cool in the presence of an applied bipolar square-wave of  $\pm 10$  V at 1 kHz. A small amount of static pressure was applied to the cell with a blunt instrument for a few seconds during the cooling process. Figure 5(c) shows optical polarizing microscope images of the cell for applied voltages of: (i)  $\pm 5$  V, (ii)  $\pm 10$  V, (iii)  $\pm 15$  V, and (iv)  $\pm 20$  V. These were taken using an Olympus BX51 with  $\times 20$  objective at 25°C on the same hot-stage. The images show that the ULH structure is well aligned with a clearly observable orientation. There is a very subtle change in color as the electric field applied increases, which is attributed to the associated reduction in birefringence.

The cell was then tested in the measurement system at a temperature of 25°C and the results are shown in Fig. 6. The AFG was programmed to apply the repeating pattern in Fig. 6(a). This pattern has a base frequency of 3 kHz and a series of bipolar pulses (increasing in amplitude from 0 to  $\pm 10$  V in 1 V increments) interspersed with  $\pm 10$  V bipolar pulses. This meant that an electric field was being continually applied to the sample to maintain the ULH structure. The varying amplitude pulses allow tilt-angle and retardance to be extracted as a function of the applied voltage from the time-resolved measurements. Figure 6(b) shows the measured tilt-angle as a function of time. It shows the flexoelectro-optic response which follows the electric field in both direction and magnitude. Previous dynamic measurements of flexoelectro-optic switching have shown the intensity variation between crossed polarizers and not shown the actual tilt-angle. A key benefit of this technique is that it gives the absolute angle over time in calibrated angular units. Thus, we obtain a true measure of the flexoelectro-optic switching over time. There is also an exceptionally low level of noise present in these measurements owing to the phase-sensitive detection used.

Figure 6(c) shows the birefringence, which was converted from the retardance measurements using the measured cell thickness and the wavelength of the He-Ne light source. It should be noted that there is an ambiguity in the measurement of the retardance which was resolved as  $\pi + \sin^{-1}()$  by knowing the approximate value of the birefringence of the ULH structure,  $\Delta n_u$ , and that the birefringence is expected to decrease with increasing electric field amplitude. This value for the birefringence also matched the color observed on the optical polarizing microscope with the corresponding color on the Michel-Levy chart, for the cell thickness of the LC device considered in this study. In Fig. 6(c), it is shown that the birefringence responds to the magnitude of the applied electric field, but it is independent of the field polarity as expected, hence the wider ‘pulses’. The magnitude of the birefringence is modulated because of the interspersed  $\pm 10$  V bipolar pulse-pairs, which reduce the birefringence to a level of around 0.0953. The in-between variable amplitude bipolar pulse pairs have birefringence values which vary from 0.0961 at 0 V down to the  $\pm 10$  V value. Also shown in Fig. 6(d) for completeness is the loss variation. This is fairly small at only 0.1 dB, but does show some structure and it has a particularly long time constant compared to the tilt-angle and birefringence changes. This is particularly evident between 6.6 ms and 7.6 ms where there is  $\pm 10$  V applied for 3 periods of the 3 kHz signal, but a slow decrease in loss. Where there are individual  $\pm 10$  V bipolar pulse pairs (e.g. 1-1.7 ms), the loss does not decrease to the same level.

Figure 7 shows the tilt-angle data from Fig. 6, but on a magnified scale, with the varying amplitude pulses overlaid. Here it can be seen that the flexoelectro-optic response is very uniform and that there is no reduction in the tilt-angle due to ionic screening effects, as the pulse durations have been kept relatively short. The well-behaved properties of this device therefore make it ideal for characterizing and proving the measurement technique. However, it should be stressed that the real value of the technique will be in the characterization of more exotic devices being operated at the limits of their performance. Here we may expect to see changes in tilt-angle, birefringence and loss with applied electric field in combination with



ionic screening. The observed behavior may well then be dependent on the particular time-domain voltage pattern applied, rather than just the instantaneous voltage. For such devices, the time-resolved measurement will be essential for accurate characterization.

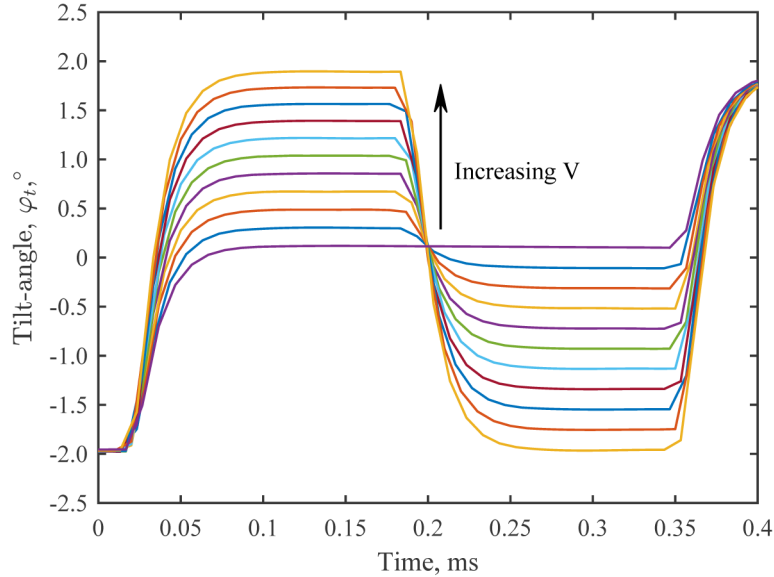


Fig. 7. Experimentally measured tilt-angle as a function of time for applied voltages from 0– $\pm 10$  V in  $\pm 1$  V increments at a temperature of 25°C and an applied frequency of 3 kHz.

## 7. Validation of dynamic switching results

It is important to establish if the experimental results under dynamic switching are in line with expectations. The same LC device was also measured using a microscope technique [15]. The same hot-stage was used, set to  $T = 25^\circ\text{C}$  as before. The sample was imaged on a polarizing microscope (Nikon OptiPhot2-Pol) using a  $\times 10$  objective and crossed polarizers. Light was collected through the phototube onto a DC coupled photodetector (Thorlabs PDA55) and the resulting voltage measured using a digitizing oscilloscope (Tektronics TDS2014). A 1 kHz bipolar square-wave was applied to the sample using the same AFG described in Section 4. Measurements were taken for a range of voltages ( $\pm 1$  V to  $\pm 10$  V in  $\pm 1$  V increments). For each applied voltage, the tilt-angle was measured as follows: The sample was rotated to find the maximum light voltage level,  $V_{\max}$ . This is where the tilt-angle during one half-cycle of the square-wave reaches the top of the  $S_0 \sin^2 2\phi \sin^2(\delta/2)$  intensity response. As this point is approached, the modulation depth is reduced and beyond it the signal distorted. Similarly, the sample was rotated back to the minimum light voltage level,  $V_{\min}$ , where the other half-cycle reaches the minimum of the intensity response. The sample was then rotated such that the modulated square-wave lies symmetrically between these two voltage levels (the  $22.5^\circ$  point). The tilt-angle was determined from the measured peak-to-peak voltage on the photodetector,  $\Delta V$ , as  $\varphi_t = \sin^{-1}((0.5 + d)^{1/2}) / 2 - \pi/8$ , where  $d = 0.5\Delta V / (V_{\max} - V_{\min})$ . This method normalizes out any field-induced birefringence changes.

Figure 8 shows a plot of  $\tan(\varphi_t)$  as a function of the applied electric field for both the microscope method and the new time-resolved method presented herein. It can be seen that the two measurement methods give very similar results, although there is clearly a small amount of scatter on the results obtained using the microscope method (note full scale is  $\sim 2^\circ$ ). However, the new method shows a very linear relationship as predicted by Eq. (18), with very

little scatter. The close agreement between the two measurements however validates the time-resolved measurement technique. From the gradient and Eq. (18), for small  $\varphi_t$  the flexoelectric ratio  $(e_1 - e_3)/(K_{11} + K_{33})$  is found to be  $0.596 \text{ CN}^{-1}$ . This figure is in very close agreement with the previously reported figure of  $0.60 \pm 0.08 \text{ CN}^{-1}$ , under the same conditions of  $T = 25^\circ\text{C}$ ,  $\lambda = 632.8 \text{ nm}$  for E7 [22].

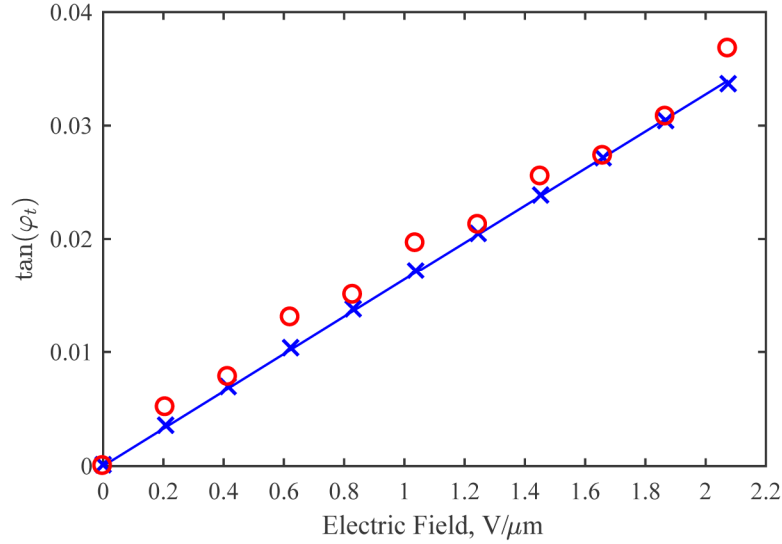


Fig. 8. Plot of  $\tan(\varphi_t)$  as a function of the electric field amplitude applied to the sample; ( $\times$  blue) data using the new time-resolved method; ( $\circ$  red) data acquired using the microscope technique.

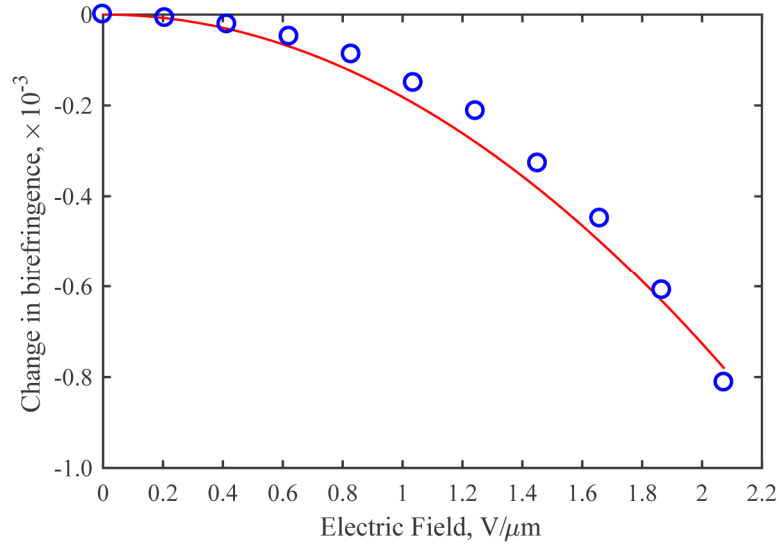


Fig. 9. Change in the linear birefringence with electric field applied to the flexoelectro-optic LC device. ( $\circ$  blue) data using the new time-resolved method, (— red) theoretical curve from Eq. (19).

In order to verify the change in birefringence determined by the new technique described in this paper, a theoretical expression for the birefringence,  $\Delta n_u$ , of a ULH structure in the presence of an applied electric field,  $E_A$  is used [23],

$$\Delta n_u = \left( \frac{n_e^2 + n_o^2}{2} \right)^{1/2} \left[ 1 - \frac{\Delta \epsilon \epsilon_0 p^2}{32 K_{22} \pi^2} \left( \frac{n_e^2 - n_o^2}{n_e^2 + n_o^2} \right) E_A^2 \right]^{1/2} - n_o \quad (19)$$

where  $n_e$  and  $n_o$  are the extraordinary and ordinary refractive indices of the intrinsic material (respectively 1.7305 and 1.5189 for E7 at  $T = 25^\circ\text{C}$  and  $\lambda = 632.8 \text{ nm}$  [21]),  $\Delta \epsilon$  is the dielectric anisotropy (14.0 for E7 at  $T = 23^\circ\text{C}$  [24]),  $\epsilon_0$  is permittivity of free space,  $p$  is the chiral pitch and  $K_{22}$  is the twist elastic coefficient (6.8 pN for E7 at  $T = 23^\circ\text{C}$  [24]). In the absence of an electric field, the second square root term disappears, giving a theoretical absolute birefringence of  $\Delta n_u = 0.1092$  for E7 at  $T = 25^\circ\text{C}$  for  $\lambda = 632.8 \text{ nm}$  light. By comparison, the measurement gives  $\Delta n_u = 0.09618$  or 11.96% error. This absolute error is larger than might be expected given the high accuracy of the test waveplate calibration and this is discussed in Section 8. The change in birefringence with applied voltage is extracted by sampling the top of the broad ‘pulses’ in the data of Fig. 6(c). This is compared to the theoretical curve obtained from Eq. (19) in Fig. 9. It can be seen that there is close correlation between the experimentally measured change in birefringence and the theoretical prediction for the device parameters.

## 8. Application to non-ideal devices

Whilst the measurement technique applies to devices which exhibit linear retardance, it is possible that non-ideality can lead to residual unwanted circular retardance. For example, in ULH devices close to the cell surfaces, there can be distortion of the helix, such that the incident light is no longer normal to the chiral nematic helix axis in these thin regions. In this event the chirality leads to circular birefringence (optical rotation). The amount of optical rotation is, however, likely to be very small. The effect of optical rotation on the measurement has been studied by adding optical rotation to Eqs. (7) and (8), and found to result in a constant offset in the absolute measured angle. The absolute angle is, however, of little consequence, as it is the switching angle which is important. Providing the magnitude of optical rotation does not change appreciably with applied field, the tilt-angle measurement is unaffected.

When ULH samples are aligned for test purposes, it is common for the helix axis orientation to vary over the surface area of the cell. Typically, the surface area may be segmented into different individual domains, with each domain having a slightly different helix orientation. A light beam entering the surface would overlap more than one such domain and it is therefore of interest to see if this measurement technique is affected when analyzing multi-domain samples. The effect of multiple domains can be analyzed by splitting the incident light into two beams of equal intensity. Each beam is propagated through the same retardance, but with the angle of the two retardances offset by  $\Delta\phi$ . The resulting intensity may then be found from

$$S_M(\theta, t) = \frac{1}{2} S_0 \left| \mathbf{P}(\theta) \left[ \mathbf{W}_D(\delta(t), \bar{\phi}(t) + \frac{1}{2}\Delta\phi) \mathbf{E}_{LC} + \mathbf{W}_D(\delta(t), \bar{\phi}(t) - \frac{1}{2}\Delta\phi) \mathbf{E}_{LC} \right] \right|^2 \quad (20)$$

where  $\mathbf{E}_{LC} = \frac{1}{\sqrt{2}} \begin{bmatrix} 1 & j \end{bmatrix}^T$  is the Jones vector for LCP light and  $\bar{\phi}(t)$  is the mean angle of the optic-axis of the two domains. Solving Eq. (20) (without assuming  $\Delta\phi$  to be small) results in the following expression

$$S_M(\theta, t) = \frac{1}{2} S_0 \left[ 1 + \sin(\delta(t)) \sin(2\theta - 2\bar{\phi}(t)) \cos \Delta\phi - \sin^2(\delta(t)/2) \sin^2 \Delta\phi \right] \quad (21)$$

This expression shows an identical phase response with  $\theta$  to that of Eq. (1), except that it is in terms of the mean angle,  $\bar{\phi}(t)$ . The tilt angle measurement is considered to be valid for samples possessing multiple domains, giving a measurement of the change in the mean angle.

There is however an error in the retardance from the change in relative fringe amplitude through Eq. (5). From Eq. (21), it can be seen that the measured  $\sin\delta$  is reduced by approximately a factor of  $\cos\Delta\phi$ . This would indicate that the sample used had some non-uniformity in helix-axis orientation, which would not be untypical for ULH alignment without using polymer stabilization or photoalignment techniques. However, the measurement system still gives the effective birefringence that would be experienced in an actual device for the beamwidth used.

## 9. Conclusions

We have demonstrated a new polarimeter which enables time-resolved measurements of both the optic-axis angle and the linear phase retardation for modulated birefringent optical devices. The measurement is fully automated and requires no angular alignment of the device under test. The time resolution is limited only by the sampling rate of the data acquisition card. A novel error cancellation scheme is used to suppress systematic error to gain a considerable improvement in accuracy. The system has been calibrated using a rotatable waveplate and shown to have an absolute angle error of  $< \pm 0.3^\circ$  and a retardance error of  $< \pm 0.44^\circ$ , with considerably better relative accuracy. For the initial demonstration, the method has been tested with a chiral nematic liquid crystal device exhibiting flexoelectro-optic switching at 3 kHz in the ULH mode. These results represent the first time-resolved tilt-angle and linear phase retardation measurements for a liquid crystal device operating at fast switching frequencies. Finally, it is shown that the measurement of the tilt-angle is also unaffected by samples exhibiting multiple domains with different orientations of the helical axis in the plane of the device. We believe that this system will have wider application in the characterization of other liquid crystal and electro-optic devices.

## Research materials

The research materials supporting this publication may be accessed at [www.eng.ox.ac.uk/smp/repository](http://www.eng.ox.ac.uk/smp/repository)

## Funding

Engineering and Physical Sciences Research Council (UK) (grant number EP/M017923/1); Royal Society University Research Fellowship.

## Acknowledgment

The authors would like to thank Dr Simon M. Wood for preparing the liquid crystal mixture.